Research Square

Preprints are preliminary reports that have not undergone peer review.
They should not be considered conclusive, used to inform clinical practice,
or referenced by the media as validated information.

Low-Background 3D Bi2WO6 Enables In Situ Sulfidation-Induced Photocurrent Polarity Switching for Highly Selective Photoelectrochemical Detection of Sulfide Ions

Zi Min
Jiangxi Agricultural University
Li Li
Jiangxi Agricultural University
Chuanfa Luo
Jiangxi Agricultural University
Chuchu Hu
Jiangxi Agricultural University
Zihan Li
Jiangxi Agricultural University
Yansha Gao
Jiangxi Agricultural University
Shaosheng Rao
Jiangxi Agricultural University
Limin Lu
lulimin816@hotmail.com

Jiangxi Agricultural University

Research Article

Keywords: Photoelectrochemical sensing, Polarity switching, 3D Bi2WO6, In situ sulfidation, S2- detection

Posted Date: August 14th, 2026

DOI: https://doi.org/10.21203/rs.3.rs-10432110/v1

License: This work is licensed under a Creative Commons Attribution 4.0 International License.
Read Full License

Additional Declarations: No competing interests reported.

Low-Background 3D Bi_2WO_6 Enables In Situ Sulfidation-Induced Photocurrent Polarity Switching for Highly Selective Photoelectrochemical Detection of Sulfide Ions

Zi Min[1], Li Li[1], Chuanfa Luo, Chuchu Hu, Zihan Li, Yansha Gao*, Shaosheng Rao*, Limin Lu*

Key Laboratory of Modern Agricultural Equipment in Jiangxi Province, Key Laboratory of Chemical Utilization of Plant Resources of Nanchang, College of Chemistry and Materials, Jiangxi Agricultural University, Nanchang, Jiangxi, 330045, China

[1]Zi Min and Li Li contributed equally to this work.

* Corresponding authors.

E-mail addresses: gaoyansha@126.com (Y. Gao), shaosheng_rao@163.com (S. Rao), lulimin816@126.com (L. Lu)

Abstract

Regulating photocurrent polarity is of significant importance for constructing photoelectrochemical (PEC) sensing platforms with enhanced sensitivity and reliability in practical applications. However, the intrinsically high background photocurrent in conventional PEC systems often masks analyte-induced signal variations, thereby hindering reliable photocurrent polarity switching. Herein, we report a low-background polarity-switchable PEC sensing platform based on three-dimensional (3D) flower-like Bi_2WO_6 for the highly selective detection of S^{2-}. Benefiting from its intrinsically low background cathodic photocurrent and hierarchical nanosheet-assembled architecture, the constructed 3D Bi_2WO_6 PEC platform exhibits a wide linear range (0-13.3 μM), a low detection limit of 16 nM outperforming the 2D Bi_2WO_6 counterpart and most previously reported PEC sensing systems for S^{2-} detection, as well as excellent anti-interference capability and reliable analytical performance in complex real samples. Mechanistic investigations reveal that the hierarchical 3D architecture facilitates local S^{2-} enrichment and accelerates the in situ surface sulfidation process, leading to the rapid formation of a direct Z-scheme Bi_2WO_6/Bi_2S_3 heterojunction. This target-triggered interfacial reconstruction dynamically reverses the dominant charge-carrier migration pathway, thereby inducing a distinct photocurrent transition from cathodic to anodic. This work provides an effective strategy for

ultrasensitive S^{2-} detection and offers new insights into the design of low-background PEC sensors with dynamically tunable signal outputs.

Keywords: Photoelectrochemical sensing; Polarity switching; 3D Bi_2WO_6; In situ sulfidation; S^{2-} detection

1. Introduction

Sulfide ions (S^{2-}), which are widely present in industrial wastewater and aquatic environments, are highly toxic pollutants that pose serious threats to ecosystems and human health even at trace concentrations[1-3]. In addition, sulfide-related compounds are commonly used in the food industry as preservatives and flavor regulators owing to their antioxidative and preservative properties. However, excessive accumulation or intake of sulfide species may adversely affect food quality and human health[4]. Therefore, the development of rapid, sensitive, and reliable analytical methods for S^{2-} detection is of great importance. Conventional techniques, including chromatography, colorimetry, and electrochemical assays, although effective, often suffer from cumbersome sample pretreatment, dependence on sophisticated instrumentation, and insufficient sensitivity[5, 6]. In recent years, photoelectrochemical (PEC) sensing has emerged as a promising analytical strategy[7-11]. By decoupling the excitation source from the signal readout, PEC sensors offer high sensitivity and rapid response, making them particularly attractive for environmental monitoring and chemical analysis[12, 13].

Despite these advantages, most conventional PEC sensors operate in a single "signal-on" or "signal-off" mode[14-17]. Such mono-directional signal outputs are highly vulnerable to fluctuations in light intensity, consumption of sacrificial agents, and interference from complex sample matrices, which may result in false-positive or false-negative responses[18-20]. To address these limitations, polarity-switchable PEC sensors, which are characterized by a distinct transition between cathodic and anodic photocurrents, have attracted increasing attention[21, 22]. This polarity-reversal behavior provides an intrinsic self-referencing capability and enhanced signal contrast, thereby significantly improving detection reliability in complex environments[23, 24].

Semiconductor heterojunctions are widely recognized as effective platforms for constructing PEC sensors[25-28]. By rationally aligning the energy band structures of different semiconductors, heterostructures can broaden light absorption and facilitate the efficient spatial separation of

photogenerated charge carriers[29-31]. For instance, a signal-switchable PEC platform based on an $Ag_2S/AgInS_2$ heterojunction has been reported, in which target-induced modulation of the interfacial charge transfer pathway enabled a polarity transition from an initially strong anodic photocurrent to a cathodic response[32]. However, conventional multi-component heterojunctions generally suffer from relatively high background photocurrents. In polarity-switchable PEC systems, such elevated baseline signals pose a critical limitation because they can obscure analyte-induced signal variations and prevent the photocurrent from crossing the zero-current threshold, thereby hindering a definitive polarity reversal. In contrast, single-component semiconductors typically exhibit lower and more stable background photocurrents, providing a favorable platform for achieving clear polarity-switching signals[33-35]. Their simplified charge transfer pathways and reduced interfacial complexity contribute to improved signal clarity and minimized background interference. Nevertheless, single semiconductors alone generally lack the capability to dynamically regulate interfacial charge transfer, which limits their ability to induce polarity transitions under conventional sensing conditions. Therefore, developing a strategy that integrates the low-background advantage of single semiconductors with the dynamic charge modulation capability of heterostructures remains a significant challenge.

In this study, we developed a polarity-switchable PEC sensing platform based on three-dimensional (3D) flower-like Bi_2WO_6 for the highly sensitive detection of S^{2-}. Benefiting from its intrinsically low background cathodic photocurrent, 3D Bi_2WO_6 provides a clear signal baseline for reliable photocurrent polarity switching. More importantly, its hierarchical nanosheet-assembled architecture facilitates local S^{2-} enrichment and accelerates the in situ surface sulfidation process, thereby enabling the rapid formation of a Bi_2WO_6/Bi_2S_3 heterointerface during sensing. This target-triggered interfacial reconstruction dynamically modulates the charge transfer pathway and induces a distinct photocurrent transition from cathodic to anodic through a direct Z-scheme charge transfer mechanism. Consequently, the constructed PEC platform exhibits a wide linear range (0-13.3 μM), a low detection limit of 16 nM, excellent anti-interference capability, and reliable analytical performance in complex real samples. Compared with the 2D counterpart, the 3D Bi_2WO_6 architecture exhibits a significantly enhanced polarity-switching response and superior detection sensitivity toward S^{2-}, achieving a detection limit superior to those of most previously reported PEC sensing systems for sulfide detection.

2. Experimental section

2.1. Materials and reagents

Bismuth nitrate pentahydrate ($Bi(NO_3)_3·5H_2O$), tungsten(VI) chloride (WCl_6), ethylene glycol (EG), and sodium sulfide nonahydrate ($Na_2S·9H_2O$) were purchased from Aladdin Biochemical Technology Co., Ltd. (Shanghai, China). Urea (CH_4N_2O) was supplied by Xilong Chemical Co., Ltd. (Guangdong, China).

2.2. Synthesis of 3D Bi_2WO_6

In a typical procedure, 260 mg of $Bi(NO_3)_3·5H_2O$ and 140 mg of WCl_6 were separately dissolved in 12.5 mL of ethylene glycol (EG) under ultrasonication at room temperature for 30 min to obtain clear solutions. Subsequently, the two solutions were mixed thoroughly, followed by the addition of 320 mg of urea. The resulting mixture was then transferred into a 50 mL Teflon-lined stainless-steel autoclave and maintained at 180 °C for 20 h. After naturally cooling to room temperature, the precipitate was collected by centrifugation, washed several times with deionized water and ethanol, and finally vacuum-dried at 60 °C to obtain 3D Bi_2WO_6 powder.

2.3. Synthesis of 2D Bi_2WO_6

The 2D Bi_2WO_6 sample was synthesized using a procedure similar to that for 3D Bi_2WO_6, except that the solvothermal reaction time was shortened to 10 h. After the reaction, the obtained precipitate was collected by centrifugation, washed several times with deionized water and ethanol, and finally vacuum-dried at 60 °C to obtain 2D Bi_2WO_6 powder.

2.4. Synthesis of Bi_2S_3

0.91 g of $Bi(NO_3)_3·5H_2O$ was dissolved in 12.5 mL of ethylene glycol (EG) to form Solution I, while 0.675 g of $Na_2S·9H_2O$ was dissolved in 15 mL of ultrapure water to form Solution II. Both solutions were ultrasonicated for 10 min to ensure complete dissolution. Subsequently, Solution II was added dropwise into Solution I under constant stirring, resulting in the immediate formation of a black precipitate. The product was collected by centrifugation and washed thoroughly with deionized water and ethanol. Finally, it was vacuum-dried at 60 °C overnight to obtain Bi_2S_3 powder.

2.5. Preparation of modified electrodes

Prior to modification, L-shaped glassy carbon electrodes (L-GCE, 5 mm diameter) were polished sequentially with 0.05 μm alumina slurry on a microcloth to a mirror-like finish, followed by rinsing alternately with ultrapure water and ethanol, and drying under ambient conditions. To fabricate the 3D

Bi_2WO_6-modified working electrode, 4.0 mg of as-synthesized 3D Bi_2WO_6 powder was dispersed in 1.0 mL of ultrapure water and sonicated for 30 min to obtain a homogeneous suspension (4.0 mg/mL). Subsequently, 15 μL of the suspension was drop-cast onto the pretreated L-GCE surface and allowed to dry at room temperature, yielding the 3D Bi_2WO_6/L-GCE electrode. Other modified electrodes (Bi_2S_3/L-GCE and 3D Bi_2WO_6/Bi_2S_3/L-GCE) were fabricated in a similar manner.

2.6. Photoelectrochemical measurements

Photoelectrochemical measurements were carried out on a CHI 660E electrochemical workstation using a standard three-electrode system, where the 3D Bi_2WO_6-modified L-GCE, a platinum wire, and an Ag/AgCl electrode functioned as the working, counter, and reference electrodes, respectively. The sensing performance was evaluated under illumination from a 300 W xenon lamp at -0.2 V bias voltage. The photocurrent response was recorded while sequentially introducing different concentrations of Na_2S and various potential interfering substances into 0.1 M Na_2SO_4 electrolyte to assess the sensitivity, selectivity, and anti-interference capability of the sensor. The operational stability was examined through repeated on/off cycles of illumination.

2.7. PEC analysis of real samples

Real samples, including lake water, tap water, egg, milk, and wine, were employed to evaluate the practical applicability of the proposed PEC sensor. Prior to analysis, lake water and tap water samples were filtered through a 0.22 μm membrane to remove suspended impurities. Egg, milk, and wine samples were appropriately diluted and pretreated to minimize matrix interference, followed by filtration through a 0.22 μm membrane. Subsequently, the standard addition method was employed by spiking known concentrations of S^{2-} into the pretreated samples. The recovery rates, calculated based on the measured and added concentrations, were used to evaluate the accuracy and reliability of the PEC sensor for complex real-sample analysis.

3. Results and discussion

3.1. Characterization of 3D Bi_2WO_6

As illustrated in Figure 1a, the 3D Bi_2WO_6 was successfully synthesized via a facile solvothermal method, and the detailed preparation process is schematically depicted. Subsequently, X-ray diffraction (XRD) analysis was performed to verify the crystal phase and purity of the as-synthesized material. As shown in Figure 1b, the obtained 3D Bi_2WO_6 exhibits distinct diffraction peaks at 2θ

values of 28.3°, 32.8°, 47.0°, 55.9°, 58.5°, and 68.8°, which can be well indexed to the (131), (200), (202), (133), (262), and (400) crystallographic planes of 3D Bi_2WO_6 (JCPDS No. 39-0256), respectively[36]. These results confirm the successful formation of 3D Bi_2WO_6, as evidenced by the absence of impurity peaks and the sharp diffraction features.

The surface morphology and structural features were investigated by scanning electron microscopy (SEM). The synthesized 3D Bi_2WO_6 exhibits a three-dimensional (3D) flower-like microsphere architecture (Figure 1c), constructed through the dense self-assembly of numerous two-dimensional (2D) nanosheets. Such a hierarchical structure provides a large specific surface area and abundant exposed active sites, which are favorable for PEC sensing[37]. For comparison in subsequent PEC measurements, a 2D Bi_2WO_6 control sample was also prepared by regulating the crystal growth process through reaction-time modulation. As shown in Figure S1, the obtained 2D Bi_2WO_6 displays a nanosheet-like morphology, providing an appropriate reference for evaluating the influence of morphology on PEC sensing performance. To further elucidate the internal structure and crystallographic characteristics, transmission electron microscopy (TEM) and high-resolution TEM (HRTEM) were performed. The TEM image (Figure 1d) is consistent with the SEM observations, revealing a spherical morphology with rough and flaky edges, which further confirms the hierarchical assembly of nanosheets. The HRTEM image (Figure 1e) displays clear and continuous lattice fringes with an interplanar spacing of 0.273 nm, corresponding to the (200) plane of Bi_2WO_6, indicating its good crystallinity[38]. Furthermore, high-angle annular dark-field scanning TEM (HAADF-STEM) coupled with energy-dispersive X-ray spectroscopy (EDS) mapping was employed to investigate the elemental distribution. As shown in Figure 1f, Bi, W, and O elements are uniformly distributed throughout the entire microsphere, demonstrating the homogeneous composition of the 3D Bi_2WO_6 architecture. The specific surface areas of the 3D and 2D Bi_2WO_6 samples were further evaluated by Brunauer-Emmett-Teller (BET) analysis. As shown in Figure S2, the 3D flower-like Bi_2WO_6 exhibits a larger specific surface area than the 2D counterpart, which can provide more exposed active sites and facilitate interfacial contact with the electrolyte during the PEC process. Overall, these results confirm the successful construction of highly crystalline 3D flower-like Bi_2WO_6 architectures with advantageous structural features for efficient charge separation and transfer in PEC sensing.

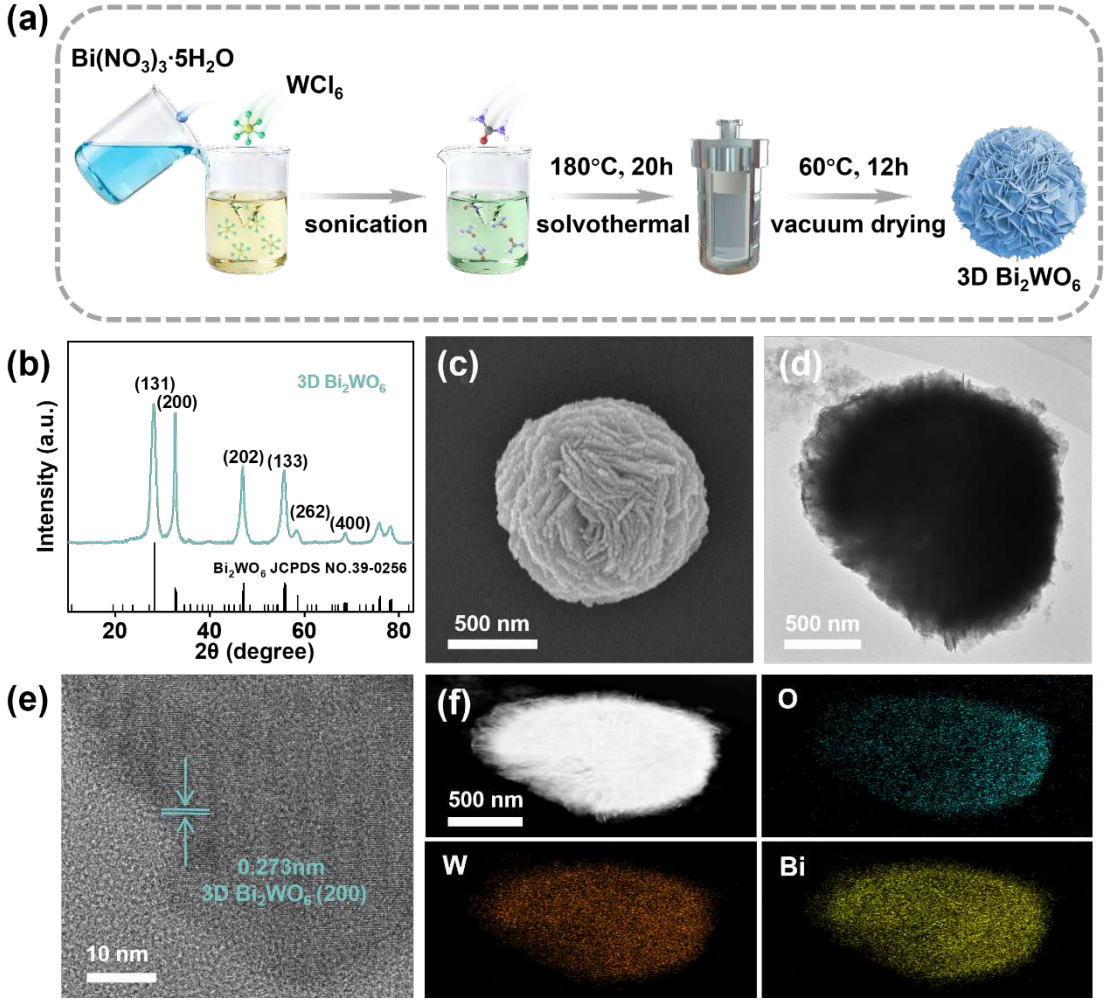


Figure 1. (a) Schematic illustration of the preparation procedure of 3D Bi_2WO_6. (b) XRD pattern, (c) SEM image of the 3D Bi_2WO_6. (d) TEM, (e) HRTEM, (f) HAADF-STEM with the corresponding EDS mapping images of 3D Bi_2WO_6.

3.2. Photoelectrochemical detection of S^{2-}

The as-synthesized 3D Bi_2WO_6 architectures were directly employed as the sensing platform. To evaluate the analytical performance of the constructed 3D Bi_2WO_6 PEC sensor, transient photocurrent responses under different conditions were systematically recorded. As shown in Figure 2a, the pristine 3D Bi_2WO_6 electrode exhibits a stable cathodic photocurrent under light irradiation, with a relatively low background current of approximately −0.1 μA. Upon the introduction of a low concentration of S^{2-} (2 μM), the cathodic photocurrent is suppressed while retaining its negative polarity. Notably, at a higher S^{2-} concentration (10 μM), the photocurrent not only increases markedly but also undergoes a distinct polarity reversal from cathodic to anodic. For comparison, the photocurrent response of the 2D Bi_2WO_6 control electrode was also investigated under identical conditions. As shown in Figure S3, the pristine 2D Bi_2WO_6 electrode likewise exhibits a stable cathodic photocurrent with a lower

background current of approximately −0.05 μA. After the addition of S^{2-}, the 2D Bi_2WO_6 electrode also displays a concentration-dependent photocurrent response and polarity transition. However, despite its lower initial background current, the photocurrent variation and signal amplification of the 2D Bi_2WO_6 electrode are significantly weaker than those of the 3D flower-like Bi_2WO_6. This result suggests that, beyond maintaining a relatively low background signal, efficient polarity-switchable PEC sensing also requires sufficient interfacial charge transfer capability and signal modulation efficiency. The enhanced PEC response of the 3D Bi_2WO_6 can be attributed to its hierarchical nanosheet-assembled microsphere architecture, which provides abundant exposed active sites and facilitates interfacial charge transfer and surface sulfidation processes. Consequently, the 3D flower-like structure enables more efficient analyte-triggered charge transfer reconstruction, leading to a more pronounced photocurrent polarity-switching behavior. These results collectively demonstrate the feasibility and superiority of the 3D Bi_2WO_6 PEC platform for polarity-switchable S^{2-} detection.

To optimize the sensing performance, key experimental parameters were systematically investigated. As shown in Figure S4a, increasing the 3D Bi_2WO_6 modification concentration from 2 to 4 mg mL^{-1} enhances the photocurrent response, owing to the increased density of accessible active sites. However, a further increase to 6 mg mL^{-1} results in a decreased photocurrent, likely due to the formation of an overly thick film that impedes charge transport and ion diffusion. Accordingly, 4 mg mL^{-1} was selected as the optimal modification concentration. The incubation time also plays a crucial role in determining sensor performance. As shown in Figure S4b, the photocurrent intensity increases with incubation time from 0.5 to 2 min and then reaches a plateau, indicating that the interfacial reaction between the electrode and S^{2-} is essentially completed within 2 min. Therefore, an incubation time of 2 min was used in all subsequent measurements.

Under the optimized conditions, the quantitative detection capability of the sensor toward S^{2-} was systematically evaluated. As shown in Figure 2b, under intermittent light irradiation, the photocurrent exhibits a clear polarity transition from cathodic to anodic with increasing S^{2-} concentration (0-13.3 μM), accompanied by a continuous enhancement of the anodic photocurrent intensity. This distinct polarity-switching behavior indicates a concentration-dependent reconstruction of the interfacial charge transfer pathway, enabling highly distinguishable signal output. Furthermore, a strong linear relationship is observed between the photocurrent density and the S^{2-} concentration. As shown in Figure 2c, the calibration plot follows the linear regression equation $y = 0.042x - 0.072$, with a

correlation coefficient (R^2) of 0.995, demonstrating the excellent quantitative detection capability of the proposed PEC sensor. For comparison, the quantitative response of the 2D Bi_2WO_6 control electrode toward S^{2-} was also evaluated under identical conditions. As shown in Figure S5a, the photocurrent response of 2D Bi_2WO_6 gradually increases with increasing S^{2-} concentration and likewise exhibits a polarity transition from cathodic to anodic. The corresponding calibration curve displays a good linear relationship over the concentration range of 0-115 μM, with a regression equation of $y = 0.0049x - 0.043$ and an R^2 value of 0.995 (Figure S5b). Notably, the slope of the 2D Bi_2WO_6 electrode is substantially lower than that of the 3D Bi_2WO_6 electrode, indicating a much weaker photocurrent response toward S^{2-} under identical conditions. This result further confirms that the hierarchical 3D flower-like Bi_2WO_6 architecture provides superior signal amplification capability and enhanced PEC sensing sensitivity. Furthermore, the limit of detection (LOD) is calculated according to the IUPAC recommendation using the equation: $LOD = \frac{3\sigma}{S}$, where σ represents the standard deviation of the blank signal and S is the slope of the calibration curve in the low-concentration region[39]. Accordingly, the LOD of the 3D Bi_2WO_6 PEC sensor was determined to be as low as 16 nM (S/N = 3). In comparison, the 2D Bi_2WO_6 control electrode exhibits a higher LOD of 145 nM under identical conditions, further highlighting the superior detection sensitivity of the 3D flower-like Bi_2WO_6 architecture. Moreover, compared with previously reported methods for S^{2-} detection (Figure 2d and Table S1), the proposed 3D Bi_2WO_6 PEC sensor demonstrates competitive analytical performance in terms of detection limit, further underscoring its high sensitivity for trace S^{2-} analysis.

Selectivity and anti-interference capability are critical parameters for evaluating the practical applicability of the 3D Bi_2WO_6 PEC sensor. A series of potential interfering anions, including $S_2O_8^{2-}$, SO_3^{2-}, SCN^-, HSO_3^-, HPO_4^{2-}, PO_4^{3-}, and NO_3^-, were systematically investigated. As shown in Figure 2e, in contrast to the pronounced anodic photocurrent response induced by S^{2-}, these interfering species only cause negligible changes in the cathodic photocurrent relative to the blank signal, which demonstrates the high selectivity of the sensor toward S^{2-}. Meanwhile, as illustrated in Figure 2f, the introduction of S^{2-} into a mixed system containing these interfering ions still results in a significant anodic photocurrent response. This observation confirms that the presence of coexisting species does not compromise the detection signal, highlighting the excellent anti-interference capability and

specific recognition of the constructed 3D Bi_2WO_6 PEC sensor toward S^{2-}. In addition, the 3D Bi_2WO_6 sensor exhibits good reproducibility across five independently prepared electrodes (Figure 2g). The operational stability was further evaluated by a continuous 10-cycle on-off light irradiation test (Figure 2h). The 3D Bi_2WO_6 electrode in the presence of S^{2-} shows negligible signal attenuation, confirming the robust stability of the 3D Bi_2WO_6 PEC sensor.

To further evaluate the practical applicability of the 3D Bi_2WO_6 PEC sensor in complex matrices, real-sample analyses were performed using filtered tap water, lake water, egg, milk, and wine samples. The standard addition method was employed by spiking known concentrations of S^{2-} (0.01, 0.1, and 1 μM) into the pretreated samples for quantitative determination. As summarized in Table S2, the recoveries range from 96.83% to 104.20%, with relative standard deviations (RSDs) between 1.46% and 3.85%. These results demonstrate that the 3D Bi_2WO_6 PEC sensor possesses excellent resistance to matrix interference and exhibits high accuracy and reliability for practical S^{2-} detection in complex real samples.

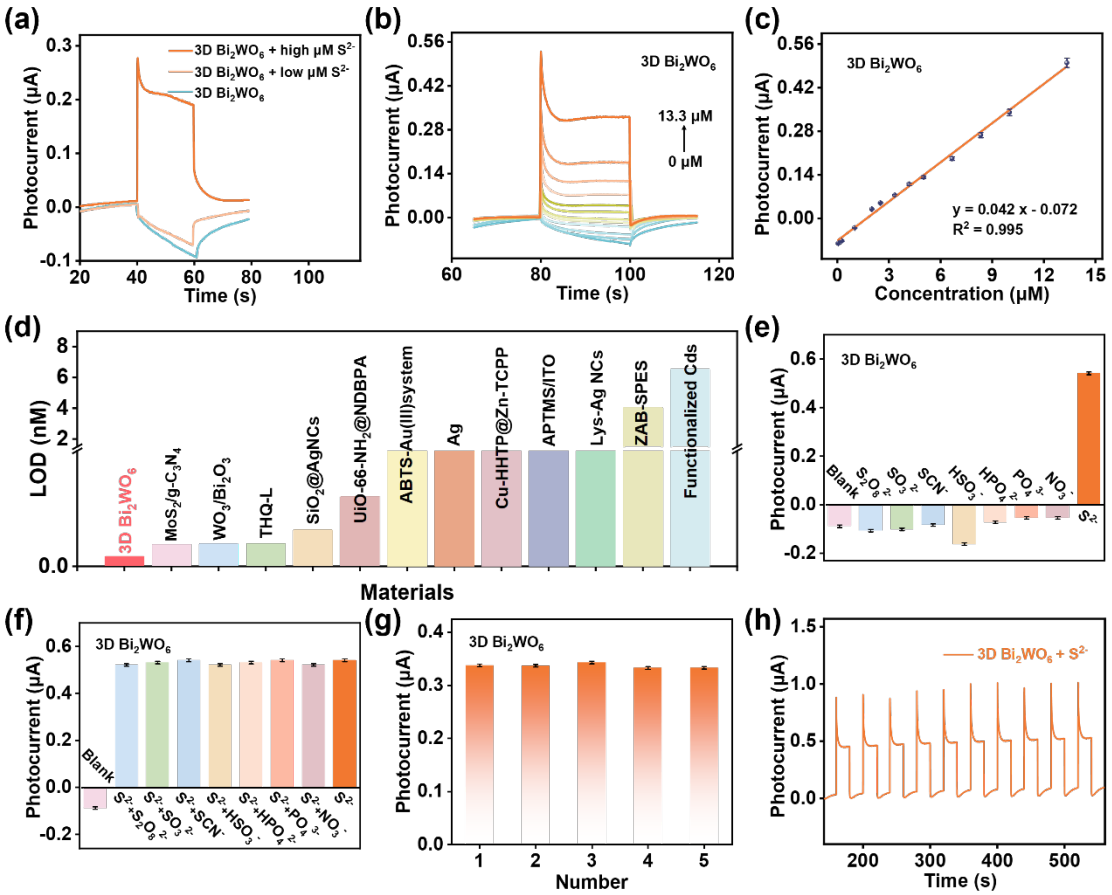


Figure 2. (a) Photocurrent responses of 3D Bi_2WO_6, 3D Bi_2WO_6 with low μM S^{2-} and 3D Bi_2WO_6 with high μM S^{2-}. (b) Photocurrent responses of 3D Bi_2WO_6 modified electrode toward different S^{2-} concentrations. (c) Linear calibration between photocurrent response and concentration of S^{2-}. (d) Comparison of the LOD for S^{2-} detection between the proposed sensor and other reported methods. (e) Selectivity of the constructed 3D Bi_2WO_6 PEC sensor

for S^{2-} sensing. (f) Anti-interference capability of the proposed 3D Bi_2WO_6 PEC sensor. (g) Reproducibility across five sensors. (h) Stability of 3D Bi_2WO_6 with S^{2-} under consecutive off-on-off light for 10 cycles.

3.3. Detection mechanism of S^{2-} at the 3D Bi_2WO_6 PEC sensor

To further elucidate the origin of the enhanced photocurrent polarity-switching behavior of the 3D Bi_2WO_6 architecture, finite element simulations were performed to compare the local S^{2-} concentration distributions around the 2D and 3D structures. As shown in Figure 3a and 3b, the 3D flower-like Bi_2WO_6 exhibits a significantly higher local S^{2-} concentration than its 2D counterpart, which can be attributed to its hierarchical nanosheet-assembled microsphere architecture with abundant exposed surfaces and enlarged interfacial contact area. Such an enhanced analyte enrichment capability is expected to accelerate the in situ surface sulfidation process and facilitate the rapid formation of the 3D Bi_2WO_6/Bi_2S_3 heterointerface. Consequently, the 3D architecture is more favorable for dynamically reconstructing the interfacial charge transfer pathway, thereby resulting in a more pronounced photocurrent polarity-switching response. Furthermore, cyclic voltammetry (CV) measurements were carried out to further evaluate the interfacial reaction behaviors of the 2D and 3D Bi_2WO_6 electrodes toward S^{2-}. As shown in Figure S6, the 3D Bi_2WO_6 electrode exhibits a stronger electrochemical response and a larger current variation than the 2D counterpart, indicating more favorable interfacial reaction kinetics and improved accessibility of active sites. This result is in good agreement with the finite element simulation, further confirming that the hierarchical 3D architecture facilitates S^{2-} enrichment and accelerates the in situ surface sulfidation process, thereby promoting dynamic reconstruction of the interfacial charge transfer pathway.

To elucidate the mechanism underlying the unique photocurrent polarity reversal, in situ Fourier transform infrared (FTIR) spectroscopy was first employed to monitor the dynamic interfacial reaction process. As shown in Figure 3c, upon the introduction of S^{2-} under light irradiation, a distinct absorption peak centered at 1200 cm^{-1} gradually emerges and continuously intensifies with reaction time. This peak is assigned to the stretching vibration of the Bi–S bond[40,41], indicating the progressive formation of Bi–S coordination during the sensing process. The time-dependent enhancement of this characteristic signal provides direct spectroscopic evidence for the in situ surface sulfidation of 3D Bi_2WO_6 induced by S^{2-}, leading to the gradual formation of a 3D Bi_2WO_6/Bi_2S_3 heterointerface. This dynamic interfacial transformation is expected to fundamentally reconstruct the charge transfer pathway, thereby contributing to the observed photocurrent polarity-switching behavior. Following

this observation, X-ray diffraction (XRD) analysis was performed to investigate the phase structure of the sample after the sensing reaction. As shown in Figure 3d, the XRD pattern of the reacted sample largely retains the characteristic diffraction peaks of pristine 3D Bi_2WO_6, indicating that the mild in situ sulfidation process does not disrupt the primary crystal framework of 3D Bi_2WO_6 and thus confirming its structural stability. Notably, a weak and broad diffraction feature appears in the 15°-27° region, which can be attributed to the formation of bismuth sulfide species (Bi_2S_3)[42]. This observation, consistent with the in situ FTIR results, suggests that S^{2-} reacts with 3D Bi_2WO_6 to induce partial surface sulfidation, resulting in the in situ generation of Bi_2S_3 on the Bi_2WO_6 surface. Such an interfacial transformation provides direct evidence that the PEC sensing mechanism is closely associated with the formation of a 3D Bi_2WO_6/Bi_2S_3 heterostructure during the sensing process.

To further investigate the chemical states, X-ray photoelectron spectroscopy (XPS) measurements were performed on both 3D Bi_2WO_6 and the reacted sample (3D Bi_2WO_6/Bi_2S_3). The XPS survey spectrum (Figure S7) reveals the emergence of a characteristic S signal in the 3D Bi_2WO_6/Bi_2S_3 sample compared with pristine 3D Bi_2WO_6, confirming the successful incorporation of sulfur species. Specifically, the high-resolution S 2s spectrum (Figure 3e) exhibits a distinct peak at 225.43 eV, which can be attributed to S^{2-} species in the Bi_2S_3 lattice, further verifying the formation of bismuth sulfide[43]. Furthermore, in the Bi 4f region (Figure 3f), two additional peaks located at 162.63 and 160.42 eV are assigned to S $2p_{1/2}$ and S $2p_{3/2}$, respectively, indicating the formation of Bi–S bonds after the reaction with S^{2-}[44]. This result provides further evidence for the in situ sulfidation process and the generation of the 3D Bi_2WO_6/Bi_2S_3 heterostructure. Notably, compared with pristine 3D Bi_2WO_6, the Bi 4f, W 4f, and O 1s spectra of the reacted 3D Bi_2WO_6/Bi_2S_3 composite all exhibit a consistent shift toward lower binding energies (Figure 3f-3h), suggesting an increased electron density around the metal centers. This shift indicates strong electronic interaction and interfacial charge transfer between 3D Bi_2WO_6 and the newly formed Bi_2S_3. These results collectively confirm that the PEC sensing process involves an in situ interfacial transformation from 3D Bi_2WO_6 to a 3D Bi_2WO_6/Bi_2S_3 heterostructure, which modulates the charge transfer pathway and ultimately contributes to the observed photocurrent polarity switching behavior.

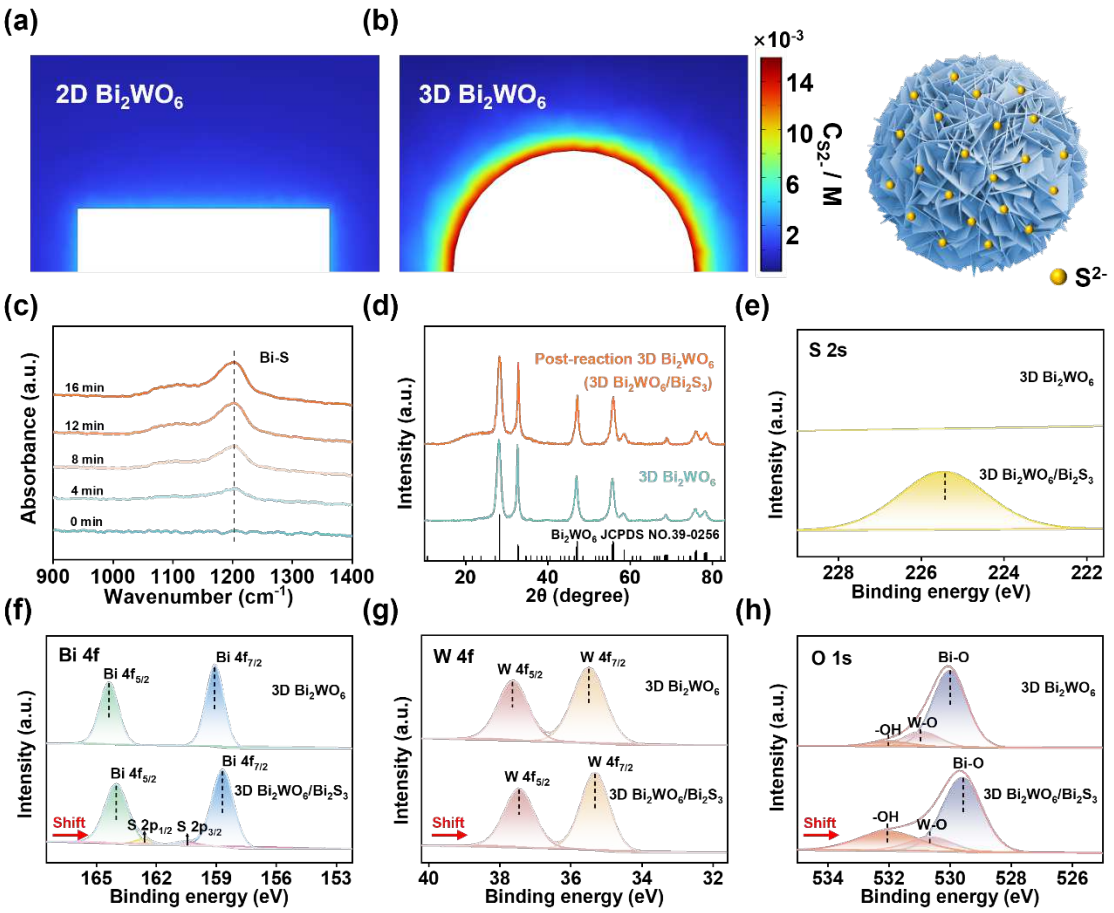


Figure 3. (a) COMSOL-simulated S^{2-} concentration distribution around 2D Bi_2WO_6. (b) COMSOL-simulated S^{2-} concentration distribution around 3D flower-like Bi_2WO_6 and schematic illustration of S^{2-}-induced in situ sulfidation to form Bi_2S_3-decorated 3D Bi_2WO_6.(c) In-situ FTIR spectra of 3D Bi_2WO_6 under different irradiation time after the introduction of S^{2-}. (d) XRD pattern of the 3D Bi_2WO_6 and 3D Bi_2WO_6/Bi_2S_3. XPS of 3D Bi_2WO_6 and 3D Bi_2WO_6/Bi_2S_3: (e) S 2s, (f) Bi 4f, (g) W 4f and (h) O 1s.

SEM was conducted to further investigate the morphological evolution after the sensing reaction. As shown in Figure 4a, compared with the pristine 3D Bi_2WO_6 exhibiting a typical 3D flower-like microsphere structure (Figure 1c), the as-formed 3D Bi_2WO_6/Bi_2S_3 heterojunction largely retains its original spherical architecture. Notably, the surface of the 3D Bi_2WO_6 nanoflowers becomes decorated with newly formed and aggregated Bi_2S_3 nanoparticles, leading to a rougher and more heterogeneous surface texture. This distinct morphological evolution provides direct visual evidence for the in-situ growth of Bi_2S_3 on the 3D Bi_2WO_6 framework, further corroborating the formation of the 3D Bi_2WO_6/Bi_2S_3 heterostructure during the sensing process.

To further confirm the in situ formation of surface Bi_2S_3 after the sensing process, the 3D Bi_2WO_6/Bi_2S_3 composite was characterized by TEM and HRTEM. The TEM image (Figure 4b) reveals a dense spherical morphology with rough edges, consistent with the SEM observations (Figure 4a), indicating that the overall architecture is well preserved after the reaction. More detailed

crystallographic information is obtained from HRTEM analysis. As shown in Figure 4c, distinct lattice fringes with interplanar spacings of 0.314 and 0.312 nm are simultaneously observed, which can be assigned to the (131) plane of 3D Bi_2WO_6 and the (211) plane of Bi_2S_3, respectively[45,46]. The clear coexistence of these two lattice domains provides direct evidence for the formation of a well-defined 3D Bi_2WO_6/Bi_2S_3 heterojunction interface via S^{2-}-induced in situ sulfidation, which is expected to modulate the interfacial charge transfer behavior. Furthermore, HAADF-STEM combined with EDS mapping was employed to probe the spatial elemental distribution. As shown in Figure 4d, Bi, W, O, and S elements are uniformly distributed throughout the entire architecture. The presence and homogeneous dispersion of S, together with Bi, W, and O, further confirm the in situ sulfidation process and the successful integration of Bi_2S_3 onto the 3D Bi_2WO_6 framework. Collectively, these structural and compositional analyses demonstrate that the sensing process induces an in situ interfacial transformation, resulting in the formation of a 3D Bi_2WO_6/Bi_2S_3 heterojunction, which modulates the charge transfer pathway and contributes to the observed photocurrent polarity switching behavior.

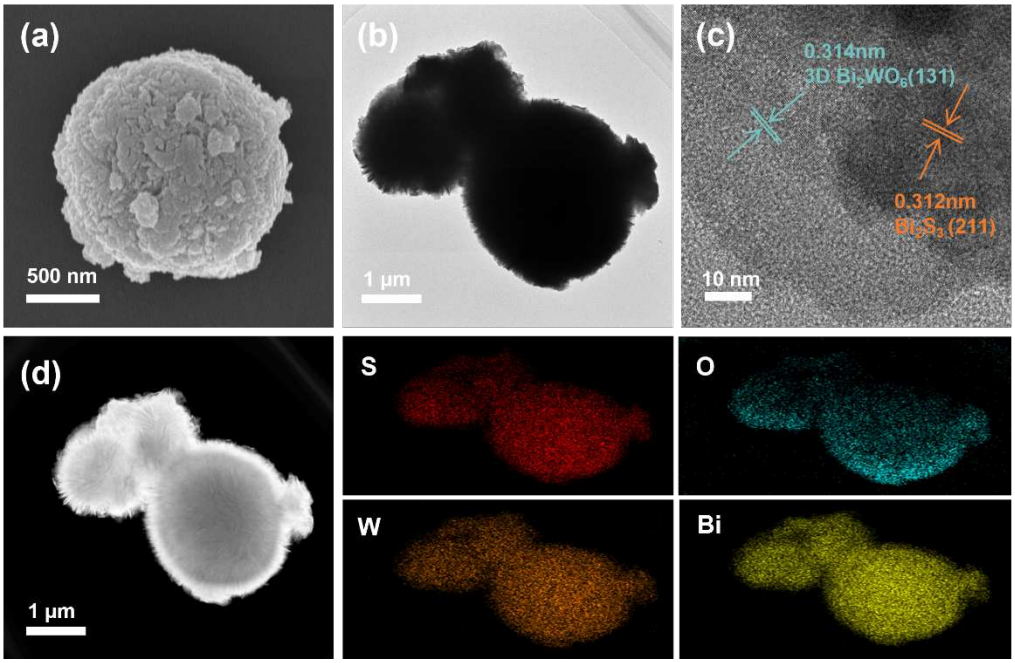


Figure 4. (a) SEM images of the 3D Bi_2WO_6/Bi_2S_3 heterojunction. (b) TEM, (c) HRTEM, (d) HAADF-STEM with the corresponding EDS mapping images of the 3D Bi_2WO_6/Bi_2S_3 heterojunction.

3.4. Mechanism of photocurrent polarity switching in the 3D Bi_2WO_6 PEC sensor

To gain deeper insight into the mechanism of photocurrent polarity switching in the 3D Bi_2WO_6 PEC sensor, the optical absorption properties and energy band structures of the materials were

systematically investigated by UV-Vis diffuse reflectance spectroscopy (UV-Vis DRS) and valence band XPS (VB-XPS). As shown in Figure 5a, pristine 3D Bi_2WO_6 exhibits strong absorption in the ultraviolet region (200-343 nm), consistent with its wide bandgap nature. In contrast, Bi_2S_3 displays broad absorption across the visible region (364-700 nm). Notably, the 3D Bi_2WO_6/Bi_2S_3 composite obtained after the sensing reaction exhibits an intermediate absorption profile, integrating features of both components. This spectral evolution indicates that the in situ formation of Bi_2S_3 on 3D Bi_2WO_6 alters the light absorption characteristics of the system. Rather than simply enhancing light harvesting, this change reflects the formation of a 3D Bi_2WO_6/Bi_2S_3 heterostructure during the sensing process, which is expected to modulate the interfacial charge transfer behavior and contribute to the observed photocurrent polarity switching. The intrinsic bandgap (E_g) of the 3D Bi_2WO_6 and Bi_2S_3 were estimated using the Tauc equation based on the Kubelka-Munk transformation:

$$(\alpha h\nu) = K(h\nu - E_g)^n \quad (1)$$

where α, hν, and K represent the absorption coefficient, photon energy, and a proportionality constant, respectively, and n depends on the nature of the optical transition[47]. For the indirect bandgap semiconductor 3D Bi_2WO_6 (n = 2) and the direct bandgap semiconductor Bi_2S_3 (n = 1/2), the corresponding E_g values are determined to be 2.45 and 1.24 eV, respectively (Figure 5b and 5c)[48,49]. To further determine the band structure, VB-XPS measurements were conducted (Figure S8a). The valence band potential versus the normal hydrogen electrode (NHE), denoted as $E_{VB\text{-}NHE}$, was calculated using the following equation:

$$E_{VB\text{-}NHE} = \Phi_x + E_{VB} - 4.4 \quad (2)$$

where Φ_x is the work function of the XPS analyzer (typically 4.4 eV), and E_{VB} is the valence band maximum extracted directly from the VB-XPS spectra[50]. Based on the results, the valence band positions of 3D Bi_2WO_6 and Bi_2S_3 are calculated to be 2.16 eV and 0.87 eV, respectively[. Accordingly, the conduction band potentials (E_{CB}) are calculated using $E_{CB} = E_{VB} - E_g$, yielding values of -0.29 eV and -0.37 eV for 3D Bi_2WO_6 and Bi_2S_3, respectively[51]. Such a staggered band alignment (Figure S8b) facilitates the directional separation and transfer of photogenerated charge carriers across the heterojunction interface, which is crucial for modulating the interfacial charge transfer pathway and ultimately contributes to the observed photocurrent polarity switching behavior.

To clarify the charge transfer direction and interfacial evolution process, ultraviolet photoelectron spectroscopy (UPS) was employed to determine the work functions (Φ) of 3D Bi_2WO_6 and Bi_2S_3,

which reflect the relative positions of their Fermi levels (E_f). As shown in Figure S9, the secondary electron cutoff energies (E_{cutoff}) of 3D Bi_2WO_6 and Bi_2S_3 are determined to be 18.30 and 18.70 eV, respectively, corresponding to work functions of 2.92 and 2.52 eV. The work function (Φ) was calculated using the following equation:

$$\Phi = h\nu - E_{cutoff} \quad (3)$$

where hν represents the photon energy of the He I source (21.22 eV)[52]. Generally, when two semiconductors come into contact, electrons spontaneously transfer from the semiconductor with a higher Fermi level (lower work function) to that with a lower Fermi level (higher work function) until equilibrium is reached. Accordingly, upon intimate contact between 3D Bi_2WO_6 and Bi_2S_3, electrons migrate from Bi_2S_3 to 3D Bi_2WO_6, resulting in the formation of an electron depletion region on the Bi_2S_3 side and an electron accumulation region on the 3D Bi_2WO_6 side. This charge redistribution establishes a built-in internal electric field (IEF) directed from Bi_2S_3 to 3D Bi_2WO_6, accompanied by band bending at the interface (Figure S10). Under light irradiation, the synergistic effect of the IEF and band bending drives the photogenerated electrons in the conduction band of 3D Bi_2WO_6 to recombine with the holes in the valence band of Bi_2S_3, leading to the formation of a direct Z-scheme charge transfer pathway. Importantly, this interfacial charge transfer mode fundamentally reconstructs the dominant charge carrier migration pathway compared with pristine 3D Bi_2WO_6, thereby inducing a transition of the photocurrent from cathodic to anodic. This charge transfer behavior is further supported by electrochemical impedance spectroscopy (EIS) and photoluminescence (PL) measurements. As shown in Figure S11, the 3D Bi_2WO_6/Bi_2S_3 heterojunction exhibits a reduced charge transfer resistance and significantly quenched PL intensity compared with pristine 3D Bi_2WO_6, indicating accelerated interfacial charge transfer and suppressed recombination of photogenerated carriers. These features collectively account for the observed photocurrent polarity switching behavior and the enhanced PEC response.

The proposed Z-scheme charge transfer pathway was further validated by electron paramagnetic resonance (EPR) spectroscopy. For DMPO-•OH radicals (Figure 5d), pristine 3D Bi_2WO_6 exhibits a discernible signal, whereas the 3D Bi_2WO_6/Bi_2S_3 heterojunction shows significantly enhanced •OH characteristic peaks, indicating that the strong oxidative holes in the valence band of 3D Bi_2WO_6 are effectively preserved. For DMPO-•O_2^- radicals (Figure S12), negligible signals are observed for pure Bi_2S_3 due to rapid intrinsic carrier recombination, while a pronounced •O_2^- signal emerges in the 3D

Bi_2WO_6/Bi_2S_3 heterojunction, demonstrating the effective utilization of high-energy electrons. From the perspective of band edge potentials, a conventional type-II heterojunction (Figure 5e, left) would lead to the accumulation of electrons in the conduction band of 3D Bi_2WO_6 (−0.29 eV) and holes in the valence band of Bi_2S_3 (0.87 eV). However, the conduction band potential of 3D Bi_2WO_6 is more positive than the standard reduction potential of $O_2/•O_2^-$ (−0.33 eV vs. NHE), and the valence band potential of Bi_2S_3 is insufficiently positive to drive the formation of $OH^-/•OH$ (+1.99 eV vs. NHE)[53]. Therefore, the type-II mechanism cannot thermodynamically account for the simultaneous generation of $•O_2^-$ and •OH, contradicting the EPR results. In contrast, the direct Z-scheme mechanism (Figure 5e, right) is well consistent with the experimental observations. Driven by the built-in internal electric field, photogenerated electrons in the conduction band of 3D Bi_2WO_6 recombine with holes in the valence band of Bi_2S_3, preserving electrons in the conduction band of Bi_2S_3 (−0.37 eV) and holes in the valence band of 3D Bi_2WO_6 (2.16 eV). This configuration not only satisfies the redox potential requirements for $•O_2^-$ and •OH generation but also fundamentally reconstructs the charge transfer pathway at the interface. More importantly, this Z-scheme-mediated charge redistribution shifts the dominant charge carrier participation from reduction-dominated processes in pristine 3D Bi_2WO_6 to oxidation-dominated processes in the heterostructure, thereby inducing the observed transition of the photocurrent from cathodic to anodic. These results collectively confirm that the S^{2-}-triggered in situ formation of the 3D Bi_2WO_6/Bi_2S_3 heterojunction governs the polarity switching behavior of the PEC response.

Based on the established direct Z-scheme heterojunction model, the mechanism underlying the unique photocurrent polarity reversal of the PEC sensor can be clearly elucidated (Figure 5f). For the pristine 3D Bi_2WO_6 electrode, under light irradiation and an applied negative bias, photogenerated electrons in the conduction band are predominantly consumed through cathodic reduction reactions, while holes in the valence band are replenished by electrons injected from the external circuit. This electron flow from the external circuit to the electrode generates a stable cathodic photocurrent. Upon the introduction of S^{2-}, an in situ surface sulfidation process is triggered, leading to the formation of Bi_2S_3 and the construction of a 3D Bi_2WO_6/Bi_2S_3 heterointerface. This interfacial transformation enables a direct Z-scheme charge transfer pathway, in which photogenerated electrons in the conduction band of 3D Bi_2WO_6 recombine with holes in the valence band of Bi_2S_3. As a result, electrons accumulate in the conduction band of Bi_2S_3, while holes are retained in the valence band of

3D Bi_2WO_6. As the heterojunction evolves, this Z-scheme pathway becomes dominant, fundamentally reconstructing the interfacial charge transfer process. The accumulated high-energy electrons in the conduction band of Bi_2S_3 are subsequently driven to flow from the photoelectrode to the external circuit, reversing the direction of electron transport. This directional inversion directly induces the transition of the photocurrent from cathodic to anodic. Therefore, the S^{2-}-triggered in situ formation of the Z-scheme 3D Bi_2WO_6/Bi_2S_3 heterojunction governs the interfacial charge transfer behavior, ultimately giving rise to the observed photocurrent polarity switching and enabling highly sensitive PEC detection of sulfide ions.

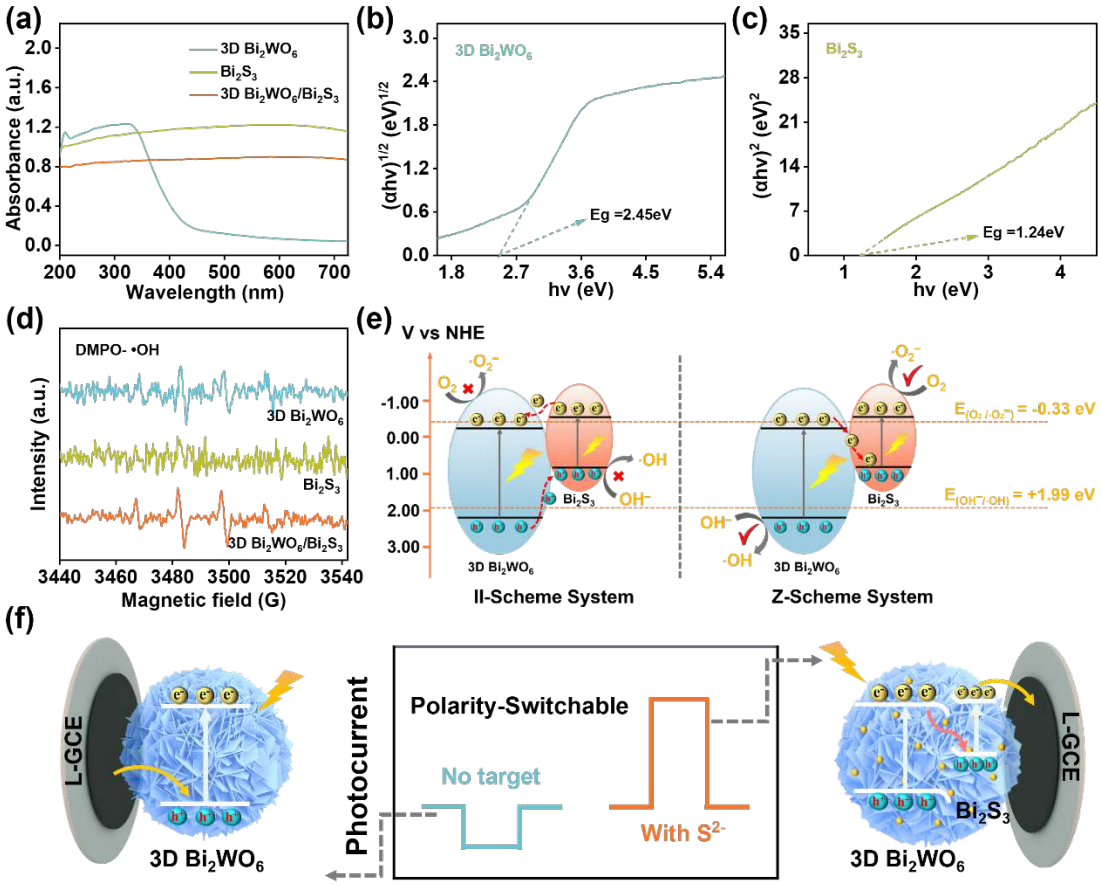


Figure 5. (a) UV-Vis DRS spectra of 3D Bi_2WO_6, Bi_2S_3, and 3D Bi_2WO_6/Bi_2S_3. (b-c) Band gaps of 3D Bi_2WO_6 and Bi_2S_3. (d) EPR spectra of DMPO-•OH radicals for 3D Bi_2WO_6, Bi_2S_3, and 3D Bi_2WO_6/Bi_2S_3 under light illumination for 5 min. (e) The schematic diagrams of the type-II and Z-scheme mechanism. (f) Schematic illustration of the polarity-switchable mechanism.

4. Conclusion

In summary, we developed a low-background polarity-switchable photoelectrochemical (PEC) sensing platform based on 3D flower-like Bi_2WO_6 for the highly sensitive detection of S^{2-}. Benefiting from its intrinsically low background cathodic photocurrent and hierarchical nanosheet-assembled

architecture, the 3D Bi_2WO_6 effectively facilitated local S^{2-} enrichment and accelerated the in situ surface sulfidation process. The dynamically formed Bi_2WO_6/Bi_2S_3 heterointerface reconstructed the interfacial charge transfer pathway through a direct Z-scheme mechanism, thereby reversing the direction of electron transport and inducing a distinct photocurrent transition from cathodic to anodic. Consequently, the proposed PEC sensor exhibited a wide linear range, a low detection limit of 16 nM, excellent anti-interference capability, and reliable analytical performance in complex real samples. Compared with the 2D counterpart, the 3D Bi_2WO_6 architecture demonstrated significantly enhanced polarity-switching behavior and superior detection sensitivity. This work provides a feasible strategy for constructing low-background, target-triggered PEC sensors with dynamically tunable signal outputs and improved analytical reliability.

CRediT authorship contribution statement

Zi Min: Experiments, Investigation, Writing–original draft, Visualization. **Li Li:** Experiments, Investigation. **Chuanfa Luo:** Investigation. **Chuchu Hu:** Investigation. **Zihan Li:** Investigation. **Yansha Gao:** Writing-review & editing. **Shaosheng Rao:** Funding acquisition, Writing-review & editing. **Limin Lu:** Supervision, Project administration, Funding acquisition, Writing-review & editing.

Declaration of competing interest

The authors declare that they have no known competing financial interests or personal relationships that could have appeared to influence the work reported in this paper.

Acknowledgements

This work was supported by the National Natural Science Foundation of China (32460628, and 22064010), the Natural Science Foundation of Jiangxi Province (20242BAB26031, and 20224BAB213009), and the PD Start-up Program from Jiangxi Agricultural University (No. 9232312034).

Appendix A. Supporting information

Supplementary data associated with this article can be found in the online version.

Reference

[1] X. Tao, X. Hu, Z. Wen, Y. a. Ming, J. Li, Y. Liu, R. Chen, Highly efficient Cr (VI) removal from industrial electroplating wastewater over Bi_2S_3 nanostructures prepared by dual sulfur-precursors: Insights on the promotion effect of sulfate ions, J. Hazard. Mater. 424 (2022) 127423.

[2] H. Wang, R. Liu, Q. Chen, Y. Mo, Y. Zhang, Biochar-supported starch/chitosan-stabilized nano-iron sulfide composites for the removal of lead ions and nitrogen from aqueous solutions, Bioresource Technol. 347 (2022) 126700.

[3] W. Zhao, H. Zhou, L. Liu, Y. Wang, S. Li, L. Guo, E. Liu, Z. Zhang, T. Sun, Porous MoS_2/Co_8FeS_8 heterojunction as bifunctional electrocatalyst for energy-saving hydrogen production coupled with sulfur recovery, Adv. Funct. Mater. 36 (2026) e19053.

[4] W. Jing, Y. Wang, Q. Shi, Y. Yang, Y. Dai, F. Liu, $Cu_2(OH)_3NO_3$ nanozyme sensor array for the discrimination of multiple sulfides in food, Biosens. Bioelectron. 262 (2024) 116529.

[5] S. Khan, J. K. Monteiro, A. Prasad, C. D. Filipe, Y. Li, T. F. Didar, Material breakthroughs in smart food monitoring: Intelligent packaging and on-site testing technologies for spoilage and contamination detection, Adv. Mater. 36 (2024) 2300875.

[6] Y. Li, X. Dong, W. Cai, Y. Liang, X. Chen, X. Li, Y. Wang, Y. Liu, H. Lei, Z. Xu, Non-toxic immunosensor for highly efficient detection of tetrodotoxin by electrochemical and colorimetric dual-mode sensing platform, Sens. Actuators B Chem. 389 (2023) 133849.

[7] Y. Chen, W. Gu, C. Zhu, L. Hu, Recent advances in photoelectrochemical sensing for food safety, Anal. Chem. 96 (2024) 8855-8867.

[8] A. Vilanova, P. Dias, T. Lopes, A. Mendes, The route for commercial photoelectrochemical water splitting: a review of large-area devices and key upscaling challenges, Chem. Soc. Rev. 53 (2024) 2388-2434.

[9] M. G. Sendeku, T. A. Shifa, F. T. Dajan, K. B. Ibrahim, B. Wu, Y. Yang, E. Moretti, A. Vomiero, F. Wang, Frontiers in photoelectrochemical catalysis: a focus on valuable product synthesis, Adv. Mater. 36 (2024) 2308101.

[10] L. Liu, X. Li, Q. Yao, Y. Hu, H. Sun, L. Zhang, J. Gong, Temperature-responsive nanocarrier-regulated alternative release of “cargos” for a multiplex photoelectrochemical bioassay of antibiotic-resistant genes, Anal. Chem. 94 (2022) 14061-14070.

[11] Y. Zi, Y. Hu, J. Pu, M. Wang, W. Huang, Recent progress in interface engineering of nanostructures for photoelectrochemical energy harvesting applications, Small 19 (2023) 2208274.
[12] P. Yang, X. Hou, X. Gao, Y. Peng, Q. Li, Q. Niu, Q. Liu, Recent trends in self-powered photoelectrochemical sensors: from the perspective of signal output, ACS Sens. 9 (2) (2024) 577-588.
[13] Z. Yang, J. Guo, L. Wang, J. Zhang, L. Ding, H. Liu, X. Yu, Nanozyme-enhanced electrochemical biosensors: mechanisms and applications, Small 20 (2024) 2307815.
[14] R. Zeng, J. Xu, T. Liang, M. Li, D. Tang, Photocurrent-polarity-switching photoelectrochemical biosensor for switching spatial distance electroactive tags, ACS Sens. 8 (2023) 317-325.
[15] L. Lu, R. Zeng, Q. Lin, X. Huang, D. Tang, Cation exchange reaction-mediated photothermal and polarity-switchable photoelectrochemical dual-readout biosensor, Anal. Chem. 95 (2023) 16335-16342.
[16] X. Chen, M. Yin, R. Ge, J. Wei, T. Jiao, Q. Chen, M. Oyama, Q. Chen, Insight into a target-induced photocurrent-polarity-switching photoelectrochemical immunoassay for ultrasensitive detection of Escherichia coli O157: H7, Anal. Chem. 95 (2023) 2698-2705.
[17] X. Wang, H. Wang, X. Wan, Q. Wei, Y. Zeng, D. Tang, Smartphone-based point-of-care photoelectrochemical immunoassay coupling with ascorbic acid-triggered photocurrent-polarity conversion switching, Biosens. Bioelectron. 267 (2025) 116749.
[18] X. Li, G. Chen, Y. Li, Y. Wang, W. Huang, G. Lai, Multiplex signal transduction and output at single recognition interface of multiplexed photoelectrochemical sensors, Anal. Chem. 96 (2024) 8147-8159.
[19] J. Xu, J. Zhang, R. Zeng, L. Li, M. Li, D. Tang, Target-induced photocurrent-polarity-switching photoelectrochemical aptasensor with gold nanoparticle-$ZnIn_2S_4$ nanohybrids for the quantification of 8-hydroxy-2′-deoxyguanosine, Sens. Actuators B Chem. 368 (2022) 132141.
[20] G. Jiang, R. Yang, J. Liu, H. Liu, L. e. Liu, Y. Wu, Two-dimensional Ti_2C MXene-induced photocurrent polarity switching photoelectrochemical biosensing platform for ultrasensitive and selective detection of soluble CD146, Sens. Actuators B Chem. 350 (2022) 130859.
[21] C. Fan, J. Lai, Z. Shao, X. Zhou, Y. Liu, Y. Lin, L. Ding, K. Wang, Target-induced photocurrent-polarity-switching PEC sensing platform based on in situ generation of oxygen vacancy-modulated energy band structures, Anal. Chem. 95 (2023) 15049-15056.
[22] Y. Chen, J. Liang, J. Xu, L. Shan, J. Lv, C. Wu, L. Zhang, L. Li, J. Yu, Ultrasensitive paper-based

photoelectrochemical biosensor for acetamiprid detection enabled by spin-state manipulation and polarity-switching, Anal. Chem. 96 (2024) 12262-12269.
[23] Y. Han, S. Jiao, X. Zhang, P. Rong, Y. Zhao, D. Jiang, W. He, D. Wang, S. Gao, J. Wang, Bipolar modulation in a self-powered ultra-wide photodetector based on Bi_2Se_3/AlInAsSb heterojunction for wavelength-sensitive imaging and encrypted optical communication, Adv. Mater. 37 (2025) 2416935.
[24] Y. Dong, N. Wang, D. Yang, J. Wang, W. Lu, D. Wang, Robust solid-liquid triboelectric nanogenerators: mechanisms, strategies and applications, Adv. Funct. Mater. 33 (2023) 2300764.
[25] J. Liu, Z. Luo, X. Mao, Y. Dong, L. Peng, D. Sun-Waterhouse, J. V. Kennedy, G. I. Waterhouse, Recent advances in self-supported semiconductor heterojunction nanoarrays as efficient photoanodes for photoelectrochemical water splitting, Small 18 (2022) 2204553.
[26] S. Zhang, H. Zheng, R. Jiang, J. Yuan, F. Li, T. Qin, A. Sakthivel, X. Liu, S. Alwarappan, Ultrasensitive PEC aptasensor based on one dimensional hierarchical $SnS_{2|}$ oxygen vacancy-WO_3 co-sensitized by formation of a cascade structure for signal amplification, Sens. Actuators B Chem. 351 (2022) 130966.
[27] X. Ren, J. Chen, C. Wang, D. Wu, H. Ma, Q. Wei, H. Ju, Photoelectrochemical sensor with a Z-scheme Fe_2O_3/CdS heterostructure for sensitive detection of mercury ions, Anal. Chem. 95 (2023) 16943-16949.
[28] H. Yang, J. Wei, J. Zheng, Q. Ai, A. Wang, J. Feng, Integration of CuS/$ZnIn_2S_4$ flower-like heterojunctions and (MnCo) Fe_2O_4 nanozyme for signal amplification and their application to ultrasensitive PEC aptasensing of cancer biomarker, Talanta 260 (2023) 124631.
[29] J. Zhang, X. Wang, X. Wang, C. Li, Heterophase junction effect on photogenerated charge separation in photocatalysis and photoelectrocatalysis, Acc. Chem. Res. 58 (2025) 787-798.
[30] M. Gu, J. Zhang, I. Kurganskii, A. Poryvaev, M. Fedin, B. Cheng, J. Yu, L. Zhang, Unveiling charge carrier dynamics at organic–inorganic S-Scheme heterojunction interfaces: insights from advanced EPR, Adv. Mater. 37 (2025) 2414803.
[31] W. Ahmad, J. Kazmi, M. Nawaz, A. Moutaouakil, J. Zhang, Y. Illarionov, Z. Wang, Interface engineering in van der Waals heterostructures: enhancing photodetector efficiency through structural and functional modifications, Adv. Funct. Mater. 36 (2026) e16893.
[32] Z. Li, J. Lu, F. Wu, M. Tao, W. Wei, Z. Wang, Z. Wang, Z. Dai, Polarity conversion of the Ag_2S/$AgInS_2$ heterojunction by radical-induced positive feedback polydopamine adhesion for signal-

590 switchable photoelectrochemical biosensing, Anal. Chem. 95 (2023) 15008-15016.
591 [33] F. Liu, J. Zhao, X. Liu, X. Zhen, Q. Feng, Y. Gu, G. Yang, L. Qu, J.-J. Zhu, PEC-SERS dual-mode
592 detection of foodborne pathogens based on binding-induced DNA walker and C_3N_4/MXene-Au NPs
593 accelerator, Anal. Chem. 95 (2023) 14297-14307.
594 [34] K. Qu, Z. Zhang, Y. Dai, X. Wang, S. Lei, X. Wang, J. Li, K. Zhang, X. Duan, X. Chen,
595 Opportunities and challenges of 2D p-type semiconductors: From material systems to electronic and
596 optoelectronic device applications, Adv. Funct. Mater. 36 (2026) e31994.
597 [35] X. Q. Yu, M. S. Wang, G. C. Guo, Single-component photochromic smart semiconductor with
598 photoswitchable fast bidirectional electron transfer, Adv. Funct. Mater. 33 (2023) 2212907.
599 [36] X. Ning, A. Hao, X. Qiu, S-Scheme heterojunction engineering of CdS/Bi_2WO_6 in breakthrough
600 piezocatalytic nitrogen reduction and hydrogen evolution: performance, mechanism, and DFT
601 calculations, Adv. Funct. Mater. 35 (2025) 2413217.
602 [37] H. Wang, J. Li, Y. Gao, X. Zheng, W. Ma, K. Cao, L. Xue, X. Li, H. Jiang, L. Wang, Boosting
603 photocatalytic H_2 evolution and benzyl alcohol oxidation via Schottky junction engineering in
604 $Cd_{9.51}Zn_{0.49}S_{10}$/Ti_3C_2 composites, J. Alloys Compd. 1059 (2026) 187158.
605 [38] Y. Chen, L. Zhang, S. Chen, S. Sun, H. Cheng, S. Li, J. Yu, B. Ding, J. Yan, Synthesis of
606 heteromorphic Bi_2WO_6 films with an interpenetrate 1D/2D network structure for efficient and stable
607 photocatalytic degradation of VOCs, Adv. Mater. 36 (2024) 2407400.
608 [39] S. Atta, Y. Zhao, J. Q. Li, T. Vo-Dinh, Dual-modal colorimetric and surface-enhanced Raman
609 scattering (SERS)-based lateral flow immunoassay for ultrasensitive detection of SARS-CoV-2 using
610 a plasmonic gold nanocrown, Anal. Chem. 96 (2024) 4783-4790.
611 [40] F. Chang, B. Lei, C. Yang, J. Wang, X. Hu, Ultra-stable $Bi_4O_5Br_2$/Bi_2S_3 np heterojunctions induced
612 simultaneous generation of radicals •OH and $•O_2^-$ and NO conversion to nitrate/nitrite species with
613 high selectivity under visible light, Chem. Eng. J. 413 (2021) 127443.
614 [41] F. Chang, W. Yan, B. Lei, X. Zhang, H. Chen, X. Hu, X. Liu, In-situ constructing Bi_2S_3
615 nanocrystals-modified $Bi_{12}O_{17}C_{l2}$ nanosheets with features of rich oxygen vacancies and reinforced
616 photocatalytic performance, Sep. Purif. Technol. 235 (2020) 116171.
617 [42] Y. Ding, Y. Li, L. Wang, B. Chai, Y. Jia, L. Sun, K. Fan, Reconstruction of Bi_2S_3 in CO_2
618 electroreduction via topotactic transformation, ACS Appl. Energy Mater. 7 (2024) 5418-5425.
619 [43] Y. Li, T. Li, Y. Deng, W. Tang, H. Wu, M. Feng, P. Yan, R. Liu, Tuning the d-band center of

620 Bi_2S_3─MoS_2 heterostructure towards superior lithium-sulfur batteries, Small 20 (2024) 2401921.
621 [44] N. Feng, Y. Wei, X. Li, Y. Zheng, R. Wei, X. Tan, J. Wu, K. Huang, Dual-polarity switching
622 photoelectrochemical biosensor based on Z-Scheme Bi_2S_3/Bi_2WO_6 heterojunction for clinical
623 thalassemia screening: cascade signal amplification via 3D DNA walker and target recycling, Anal.
624 Chem. 97 (2025) 23640-23649.
625 [45] Y. Zhang, Y. Li, Y. Yuan, Carbon quantum dot-decorated BiOBr/Bi_2WO_6 photocatalytic
626 micromotor for environmental remediation and DFT calculation, ACS Catal. 12 (2022) 13897-13909.
627 [46] Y. Li, J. Chen, S. Chen, T. Lu, X. Liao, T. Zhao, F. Cheng, H. Wang, Proton-rich two-dimensional
628 defective Bi_2S_3-derived nanosheets for boosting CO_2 electroreduction, Appl. Catal. B Environ. Energy
629 349 (2024) 123874.
630 [47] S. Rao, Z. Lu, J. Xie, Z. Li, H. Liu, X. Yu, Q. Liu, J. Yang, Atomic Zn-N_4 site-regulated donor-
631 acceptor catalyst for boosting photocatalytic bactericidal activity, Nano Lett. 24 (2024) 15598-15606.
632 [48] D. Peng, H. Zeng, J. Xiong, F. Liu, L. Wang, S. Xu, Z. Yang, S. Liu, Tuning oxygen vacancy in
633 Bi_2WO_6 by heteroatom doping for enhanced photooxidation-reduction properties, J. Colloid Interface
634 Sci. 629 (2023) 133-146.
635 [49] Z. Zhao, X. Li, K. Dai, J. Zhang, G. Dawson, In-situ fabrication of Bi_2S_3/$BiVO_4$/$Mn_{0.5}Cd_{0.5}S$-
636 DETA ternary S-scheme heterostructure with effective interface charge separation and CO_2 reduction
637 performance, J. Mater. Sci. Technol. 117 (2022) 109-119.
638 [50] H. Wang, J. Li, Z. Jiao, X. Zheng, W. Ma, K. Cao, L. Xue, F. Xu, Y. Wan, Y. Yang, B. Li, P. Huo,
639 Dual-redox cycling driven charge transfer in Cu_xO/CeO_2 heterojunction for photocatalytic activation
640 of peroxymonosulfate toward tetracycline degradation, J. Colloid Interface Sci. (2026) 139996.
641 [51] S. Rao, Z. Sun, Q. Liu, C. Cheng, C. Jin, J. Gao, B. Li, Y. Li, L. Liu, J. Yang, Y. Zhu, Engineering
642 atomic Ag_1-N_6 sites with enhanced performance of eradication drug-resistant bacteria over visible-
643 light-driven antibacterial membrane, ACS Nano 18 (2024) 7074-7083.
644 [52] N. Li, J. Zhang, J. Ma, C. Xue, Q. Chang, L. Liu, X. Fan, C. Hao, S. Wang, S. Hu, Efficient
645 photocatalytic hydrogen evolution enabled by defect-and interface-induced dual built-in electric fields
646 in a $ZnIn_2S_4$/1T-2H WS_2 heterojunction, Small (2026) e14954.
647 [53] H. Guo, S. Wang, X. Chen, J. Kou, G. He, Z. Dong, Y. Yan, Engineering a covalent organic
648 framework-based type-II heterojunction for enhanced photocatalytic H_2O_2 synthesis, Nat. Synth. 4
649 (2025) 1610-1620.

Supplementary Files

This is a list of supplementary files associated with this preprint. Click to download.

- Supportinginformation.docx